Article

Super Resolution Mapping of Scatterometer Ocean Surface Wind Speed Using Generative Adversarial Network: Experiments in the Southern China Sea

Xianci Wan [1], Baojian Liu [2,*], Zhizhou Guo [1], Zhenghuan Xia [3], Tao Zhang [3], Rui Ji [1] and Wei Wan [1,*]

[1] Institute of Remote Sensing and GIS, School of Earth and Space Sciences, Peking University, Beijing 100871, China; wanxianci@stu.pku.edu.cn (X.W.); zzguo@pku.edu.cn (Z.G.); toplane@pku.edu.cn (R.J.)
[2] School of Soil and Water Conservation, Beijing Forestry University, Beijing 100083, China
[3] State Key Laboratory of Space-Ground Integrated Information Technology (SKL-SGIIT), Beijing Institute of Satellite Information Engineering, Beijing 100095, China; maxwell_xia@126.com (Z.X.); forzhangtao@163.com (T.Z.)
[*] Correspondence: liubaojian@pku.edu.cn (B.L.); w.wan@pku.edu.cn (W.W.)

Abstract: This paper designed a Generative Adversarial Network (GAN)-based super-resolution framework for scatterometer ocean surface wind speed (OSWS) mapping. An improved GAN, WSGAN, was well-trained to generate high-resolution OSWS (~1/64 km) from low-resolution OSWS (~12.5 km) retrieved from scatterometer observations. The generator of GAN incorporated Synthetic Aperture Radar (SAR) information in the training phase. Therefore, the pre-trained model could reconstruct high-resolution OSWS with historical local spatial and texture information. The training experiments were executed in the South China Sea using the OSWS generated from the Advanced SCATterometer (ASCAT) scatterometer and Sentinel-1 SAR OSWS set. Several GAN-based methods were compared, and WSGAN performed the best in most sea states, enabling more detail mining with fewer checkerboard artifacts at a scale factor of eight. The model reaches an overall root mean square error (RMSE) of 0.81 m/s and an overall mean absolute error (MAE) of 0.68 m/s in the collocation region of ASCAT and Sentinel-1. The model also exhibits excellent generalization capability in another scatterometer with an overall RMSE of 1.11 m/s. This study benefits high-resolution OSWS users when no SAR observation is available.

Keywords: scatterometer; ocean surface wind speed; super-resolution; GAN

1. Introduction

Ocean surface wind stands as a crucial air-sea interface variable [1]. Large-scale and high-resolution (HR) ocean surface wind speed (OSWS) is required for scientific research and operational applications [2]. For example, it plays an influential role in ocean-atmosphere coupled modeling [3], marine renewable energy assessment [4], marine spatial planning [5], and disaster monitoring [6]. So far, the confident global OSWS product, such as ERA-5, is mainly based on the spaceborne scatterometer at spatial resolutions varying from 12.5 to 50 km [7]. When more detailed wind speed information is necessary, the synthetic aperture radar (SAR) is sufficient in spatial resolution but insufficient in spatial coverage [1]. Therefore, the abovementioned applications will benefit from a finer-resolution, easily available wind speed map.

In the last several years, generative adversarial networks (GAN) [8] have achieved a milestone advancement in image processing [9]. A previous study first introduced GAN into image super-resolution, Super-Resolution GAN (SRGAN) [10], which exploited residual network structure as the main structure for the generator and employed an adversarial loss term for visually pleasing results. With the development of SRGAN, GANs have demonstrated their ability to produce excellent outcomes in super-resolution. Due

to the improvement in the network architecture, adversarial loss, and perceptual loss, Enhanced SRGAN (ESRGAN) [11] could better alleviate the artifacts compared to SR-GAN. Single Image Super-Resolution with Feature Discrimination (SRFeat) network [12] added a feature discriminator to eliminate high-frequency noise. GAN-based Single Image Super-Resolution with Dual Discriminator and Channel Attention (GDCA) network [13] improved the generator of SRFeat with multiple residual channel attention blocks for better mining of higher-level features. The remote sensing community has adopted SRGAN and its variants and reported successful use in various tasks, such as pothole detection [14], sea surface temperature [15], land cover classification [16], and aerosol optical depth estimation [17]. It is reasonable to predict that the well-trained generator will restore a satisfied HR scatterometer OSWS by excavating the exact spatial feature in HR SAR reference OSWS and learning some historical local spatial and texture information [18].

For the OSWS super-resolution mapping, the existing architecture of super-resolution GAN models designed for computer vision cannot be directly applied. The two main reasons are as follows. Compared to commonly used computer vision datasets, remote sensing datasets are considered small datasets, especially those focused on the collocation observation of SAR and scatterometer. Therefore, some complex deep networks may not be suitable for the OSWS super-resolution mapping [19]. Additionally, this research aims to enable the scatterometer OSWS to learn local historical spatial information from SAR OSWS while preserving the OSWS inversion accuracy of the scatterometer itself. Unlike traditional computer vision, OSWS super-resolution belongs to quantitative remote sensing, and while striving for high resolution, maintaining the accuracy of the grayscale values in the OSWS images is also a key that should be considered.

This study aims to design a GAN-based framework, achieving the HR scatterometer OSWS mapping from the LR OSWS retrieval from scatterometer observations based on the existing geophysical model function (GMF). To fit OSWS's characteristics, wind speed GAN (WSGAN) was developed in this study, adjusting the generator of ESRGAN in convolutional kernels and the number of residual blocks, improving the original discriminator of ESRGAN, and applying feature GAN loss of SRFeat to retain the accuracy of scatterometer wind fields while learning the historical spatial features of SAR wind fields. The experiments were first conducted in the South China Sea using the Advanced SCATterometer (ASCAT) scatterometer and Sentinel-1 SAR OSWS set and then extended to apply to the scatterometer data from Wind Radar (WindRAD) on board Fengyun-3E (FY-3E). The ESRGAN, SRFeat, GDCA, Enhanced Deep Super-Resolution (EDSR) [20], Residual Channel Attention Network (RCAN) [21], Laplacian Pyramid Super-Resolution Network (LapSRN) [22], and Multi-scale Residual Network (MSRN) [23] models were applied as comparison methods and exhibited competent results.

2. Data and Methods

This study focuses on the super-resolution mapping of scatterometer OSWS using GAN in the Southern China Sea. The ASCAT and WindRAD scatterometer data at low resolution (0.125°) were applied to train and test the GAN model, while the Sentinel-1 SAR data as a high-resolution (1/64°) reference. Then, a well-trained GAN model was used to generate the higher-resolution scatterometer OSWS at eight scale factors.

Due to the complex marine dynamic environment and the unique geographical location, the Southern China Sea is suitable for OSWS studies [24]. 11,575 ASCAT L2B wind field data and 2755 Sentinel-1 L2 IW OCN data were downloaded, covering the South China Sea from 28 October 2017 to 3 September 2022. The data matching strategy is as follows: ensure a temporal difference in acquisition times between ASCAT and Sentinel-1 of less than 3 h, a collocation area exceeding $100 \times 100 \text{ km}^2$, and a proportion of missing wind speed pixels less than 1%. Due to the non-coincidence of the orbits of ASCAT and Sentinel-1, 182 ASCAT L2 data and the spatiotemporal corresponding Sentinel-1 L2 wind speed products were finally matched and selected to produce the OSWS sets. Three pairs of images from 2019, 2020, and 2021 and ten pairs from 2022 were selected for the test set

and the rest for the train and validation sets. Due to the uneven spacing of wind speed data in both latitude and longitude from ASCAT and Sentinel-1, it is necessary to interpolate them into a standardized grid. The spatial resolutions of OSWS images from SAR and scatterometer were resampled to 0.125° and 1/64° (i.e., 8:1) using bilinear interpolation, respectively. To enhance the number of samples in both the training and validation datasets, the starting latitude and longitude of the regular grid were adjusted while maintaining the grid's latitude and longitude intervals. Specifically, each grid's starting longitude and latitude were increased by 0.0125° and iterated 21 times. After augmentation, selection, and segmentation, there are 2686 pairs of OSWS images covering the collocation area of the ASCAT and Sentinel-1 in the train set and 671 pairs in the valid set. The sizes of the OSWS image patches of ASCAT and Sentinel are 8×8 and 64×64 pixels, respectively. The newly launched WindRAD L1 data is available only from 15 March 2022, which leads to insufficient SAR data for spatiotemporal collocation and subsequent training. Hence, 30 WindRAD L1 10 km data observations recorded in 2022 were chosen to evaluate the model's performance.

2.1. Data

2.1.1. ASCAT L2B Data

The ASCAT enables the acquisition of timely normalized radar cross-section (NRCS) measurements with a specified spatial sampling of 25 km. The swath width of ASCAT is 512.5 km [25]. The ASCAT operates in the C-band (approximately 5.3 GHz) with VV polarization and employs six fan-beam antennas (each satellite side with three antennas) to observe ocean surface data. ASCAT L2B data provided by the European Space Agency (ESA) contains the stress equivalent to 10 m winds (speed and direction) retrieved by COMD7 [25]. The spatial resolution of winds is 12.5 km.

2.1.2. WindRAD L1 Data

WindRAD is the inaugural dual-frequency, four-antenna rotating fan-beam scatterometer installed on FY-3E, China's second-generation sun-synchronous polar-orbiting meteorological satellite. As an improvement, the geometry of view azimuth and incidence angles of WindRAD are highly varied across the swath. In each Wind Vector Cell (WVC), WindRAD significantly increases the number of views compared to that of ASCAT, with up to 30 views. Operating in both C-band (approximately 5.4 GHz) and Ku-band (approximately 13.256 GHz), WindRAD utilizes VV and HH polarization [26]. The Level-1 data from WindRAD provided by the Chinese National Satellite Meteorological Center (NSMC) incorporates two distinct WVC sizes: 20 km $\times$ 20 km and 10 km $\times$ 10 km, corresponding to 70 WVCs and 140 WVCs across the swath, respectively [27].

2.1.3. Sentinel-1 L2 IW OCN Data

The Sentinel-1 satellites are equipped with a C-band (5.405 GHz) SAR side-looking radar instrument. They provide Ground Range Detected Interferometric Wide-swath (IW) backscatter observations in polarization (VV and VH) with a ground swath width of 250 km and a spatial resolution of 20 m [28]. The revisit time for one Sentinel satellite is 12 days. The Level 2 IW OCN data provided by ESA offers a gridded ground range estimate for the surface wind speed and direction at 10 m above the surface. This information is derived from IW mode at 1 km spatial resolution.

2.1.4. ECMWF ERA-5 Reanalysis Wind Speed

European Centre for Medium-Range Weather Forecasts (ECMWF) provides ERA-5 reanalysis data, which is generated by the combination of 4D-Var data assimilation and model forecasts [29]. The ERA-5 reanalysis wind speed product offers the analyzed 10 m wind components, including wind speed and direction, at 12.5 km resolution [30]. This data could serve as validation data, which is reliable when wind speed is below 30 m/s.

2.2. Methods

As illustrated in Figure 1, the design of the proposed method is to achieve the HR scatterometer OSWS mapping using a developed GAN model from the LR OSWS retrieval from scatterometer observations based on the exited GMF using maximum likelihood estimation (MLE). Therefore, the relative GMF, the proposed WSGAN model, and the SRGAN variants used for comparison were mainly introduced in this section.
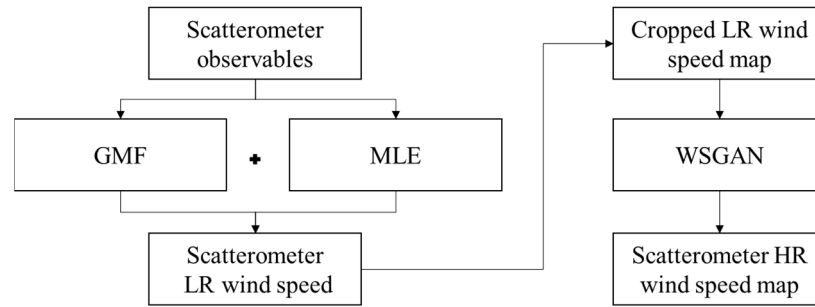

Figure 1. The flow of the designed GAN-based method for super-resolution mapping of scatterometer OSWS.

2.2.1. GMF

GMFs are semi-empirical methods that yield σ_0 by correlating with wind speed V, wind direction concerning beam azimuth ϕ, and antenna incidence angle θ. The GMFs are commonly applied by scatterometers [30–32] and SAR [33–35] to retrieve OSWS using MLE estimators. Some GMFs were initially developed only for the C-band scatterometer data operating in VV polarization, such as ASCAT, commonly referred to as CMOD. The state-of-the-art CMOD is CMOD7 [25], which is also the official algorithm to provide ASCAT and WindRAD L2 wind speed products. A C-band VV-polarised GMF can be modeled as follows:

$$\sigma_0(\theta, V, \phi) = B_0(V, \theta) \left[1 + B_1(V, \theta) \cos(\phi) + B_2(V, \theta) \cos(2\phi)\right]^n \tag{1}$$

where σ_0 represents the NRCS; θ, V, and ϕ are the local magnitudes representing the incidence angle of radar, the OSWS at the reference elevation of 10 m, and the ocean surface wind relative direction.

2.2.2. The Proposed WSGAN

The single-channel OSWS images have a distinct characteristic: relatively lower contrast and sparse features. This aspect makes the original structure of the SRGAN, which was designed with color images in mind, inappropriate for their processing. However, there is a silver lining, as the evolution of SRGAN variants opens up opportunities for OSWS super-resolution restoration. This refinement process primarily focuses on the generator, the discriminator, and the loss function. Regarding the generator, some network designs lean towards incorporating complexity layers for advanced information mining. Others, however, choose to eliminate superfluous structures, resulting in a more lightweight network. The latter strategy is deemed more fitting for this study due to the constraints imposed by the size of the available datasets. A similar approach is utilized in the design of the discriminator. While some GAN architectures feature dual discriminators, the potential advantage of an additional feature discriminator, such as yielding more informative insights, is offset by its increased challenge in model training. Hence, a streamlined, lightweight discriminator is preferred.

Figure 2 illustrates the architectural framework of WSGAN. Its generator integrates the Residual-in-Residual Dense Block, removes Batch Normalization (BN) layers, and uses residual scaling and smaller initialization, resembling the ESRGAN structure. The number of convolutional kernels and the number of residual blocks have been adjusted to better align with the unique requirements of the OSWS dataset, which were set to 16 and 3×3.

Despite the adjustments made in ESRGAN's discriminator, WSGAN did not incorporate these alterations. Instead, the discriminator of WSGAN employs 3×3 convolutional kernels, organized in blocks with kernel counts of 64, 64, 128, 128, 256, and 256, and incorporates BN and Leaky ReLu layers. The fundamental objective of WSGAN is the reconstitution of OSWS by assimilating SAR information. Therefore, the revision in the discriminator of ESRGAN seems extraneous. The enhancements above significantly boost WSGAN's training efficiency. More importantly, they equip WSGAN with an increased capacity to restore more detailed and nuanced OSWS.
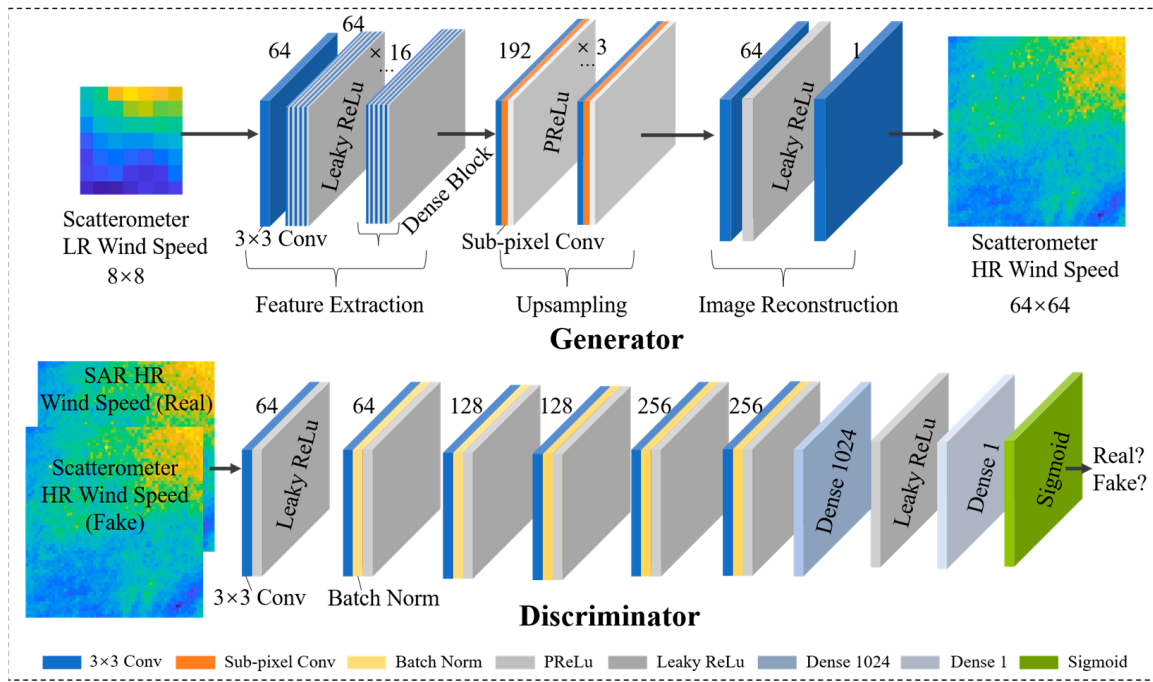

Figure 2. The architecture of WSGAN. Different colors indicate distinct modules, with specific corresponding module names already labeled.

The generator network was trained through pre-training and adversarial training, and the loss function is a crucial component. During pre-training, the generator was trained by minimizing an MSE loss [12]:

$$\frac{1}{W_m H_m C_m} \sum_i^{W_m} \sum_i^{H_m} \sum_i^{C_m} \left(\phi_{i,j,k}^m \left(I^h \right) - \phi_{i,j,k}^m \left(I^g \right) \right)^2 \tag{2}$$

where W_m, H_m, and C_m denote the dimensions of the m-th feature map ϕ^m. ϕ^m represents the output of the ReLU layer after the convolution before the m-th pooling, I^h denotes the original high-resolution image, I^g denotes the corresponding super-resolution image.

The GAN framework endeavors to solve the minimax problem defined as follows [10]:

$$\min_g \max_d \left(\mathbb{E}_{y \sim p_{\text{data}}(y)} [\log d(y)] - \mathbb{E}_{x \sim p_x(x)} [\log(1 - d(g(x)))] \right) \tag{3}$$

where $x \in X$, $y \in Y$, generator g generates images $g(x)$ by learning the mapping from X to Y; discriminator d, on the other hand, learns features of Y and $g(x)$ to distinguish whether the images are authentic or generated by g; the objective of g is to minimize this loss, while d aims to maximize it.

Inspired by the feature GAN loss of SRFeat [12], the loss function applied in adversarial training is as follows:

$$\begin{cases} L_g = L_p + \lambda L_a \\ L_p = \frac{1}{W_m H_m C_m} \sum_i^{W_m} \sum_i^{H_m} \sum_i^{C_m} \left(\phi_{i,j,k}^m \left(I^h \right) - \phi_{i,j,k}^m (I^g) \right)^2 \\ L_a = -\log\left(d\left(\phi^m \left(I^h \right) \right) \right) - \log(1 - d(\phi^m(I^g))) \end{cases} \quad (4)$$

where L_p and L_a represent the perceptual and adversarial losses, λ is a weight for the GAN loss terms.

L_a aims to guide the generator in synthesizing structural intricacies within the feature domain, diverging from the conventional SRGAN variants that primarily focus on generating high-frequency details at the pixel level. By encoding structural information within the feature map, the discriminator distinguishes between super-resolved images and genuine high-resolution images, relying not solely on high-frequency information but also on structural information. Then, our goal, which is to retain the accuracy of scatterometer wind fields while learning the historical spatial features of SAR wind fields, is achieved by minimizing the loss function in adversarial training.

2.2.3. SRGAN Variants Used for Comparison

Several SRGAN variants, i.e., ESRGAN, EDSR, GDCA, SRFeat, RCAN, LapSRN, and MSRN, introduced in this section, were exercised in the experiment as a comparison. In terms of the improved generators, EDSR is an enhanced deep residual network that eliminates the conventional residual architecture, enabling the extraction of deeper features. This modification aids in capturing more intricate details during the training process. LapSRN efficiently employs the Laplacian pyramid to capture image details across various scales, demonstrating proficiency in preserving intricate features. MSRN leverages multiple-scale residual blocks, adeptly capturing both global and local features. RCAN introduces residual channel attention blocks, allowing deep network training with exceptional performance. RCAN enhances the model's ability to focus on essential features by incorporating attention mechanisms, resulting in better output quality. SRFeat incorporates a feature discriminator and employs adversarial loss terms. These additions contribute to eliminating high-frequency noise, resulting in cleaner and more realistic output images. Building upon SRFeat, GDCA further improves the generator by employing multiple residual channel attention blocks. This approach is particularly suitable for learning higher-level OSWS features with more significant non-linearity and larger receptive fields. ESRGAN introduces several enhancements to the network structure. It embraces the residual-in-residual dense block, eliminates BN layers, and incorporates innovative techniques such as residual scaling and smaller initialization. These significant modifications yield remarkable performance enhancements and produce visually captivating results. The pros and cons of the mentioned models are summarized in Table 1.

2.2.4. GAN Model Hyperparameter Setting

The training of the above GAN-based models includes generator pre-training and generator-discriminator GAN training. During the two training phases, the parameters were all optimized by adaptive moment estimation (Adam), and all the initial learning rates of the generators were set to 1×10^{-4}. Their learning rate decay was adjusted to 0.1 and 0.5, individually. The above GAN-based models were trained for 500 and 20 epochs, respectively, with the batch size set to 8. The above GAN models were implemented on a single NVIDIA Tesla P100 GPU.

Table 1. The pros and cons of the super-resolution models.

Models	Pros	Cons
SRGAN [10]	Produces visually appealing images with fine textures by introducing GAN.	Prone to artifacts and overfitting during training.
ESRGAN [11]	Improves feature extraction capability and perceptual loss for enhancing image quality	May generate artifacts and over-smoothing.
GDCA [13]	Enhances super-resolution performance by using residual connections and channel attention modules.	Requires a significant amount of computational resources and time for training and inference.
SRFeat [12]	Improves high-frequency information and structural information extraction capability.	Increases the complexity and computational load of the limited performance on complex image structures.
EDSR [20]	Emphasizes deep networks with residual connections for effective feature learning.	Requires substantial computational resources during training
RCAN [21]	Enhances the model's ability to focus on essential features by incorporating attention mechanisms.	Training may still be resource-intensive.
LapSRN [22]	Efficient use of the Laplacian pyramid to capture image details at different scales; Good at preserving fine details.	Limited in handling large upscaling factors.
MSRN [23]	Utilizes multiple-scale residual blocks to capture both global and local features.	May struggle with extremely low-resolution inputs.

2.2.5. Accuracy Evaluation

The accuracy evaluation of OSWS retrievals commonly employs the root mean square error (RMSE) [36,37] as a metric. In addition, mean absolute error (MAE) [37,38] and symmetric mean absolute percentage error (SMAPE) [39,40] were selected as the accuracy metrics. The ERA-5 Reanalysis Wind Speed product provides analyzed 10 m wind speed and wind direction with a resolution of 12.5 km [30], typically considered a reliable reference data source for comparison. The definition of RMSE, MAE, and SMAPE is as follows:

$$\text{RMSE} = \sqrt{\frac{\sum_{i=1}^{N} (WS_{SR} - WS_{ERA})^2}{N}} \tag{5}$$

$$\text{MAE} = \frac{\sum_{i=1}^{N} |WS_{SR} - WS_{ERA}|}{N} \tag{6}$$

$$\text{SMAPE} = \sum_{i=1}^{N} \frac{|WS_{SR} - WS_{ERA}|}{(|WS_{SR}| + |WS_{ERA}|)/2} \times \frac{100\%}{N} \tag{7}$$

where WS_{SR} and WS_{ERA} represent the super-resolution OSWS and the upsampled ERA-5 OSWS separately, and N represents the number of collocated pixels.

3. Results and Discussions

3.1. Performance of WSGAN on Achieving High-Resolution Wind Speed

Figure 3 shows the OSWS restoration results on 28 January 2022, 10 April 2022, and 18 August 2022, at a scale of 8. The RMSE, MAE, and SMAPE of the above methods in different OSWS segments on the collocation regions of ASCAT and Sentinel-1 are depicted in Table 2, Table 3, and Table 4, respectively. The overall accuracy comparison is depicted in Figure 4. Notably, the ERA-5 used the ASCAT observations in the data assimilation, and the accuracy in this study is a proxy rather than a real error.
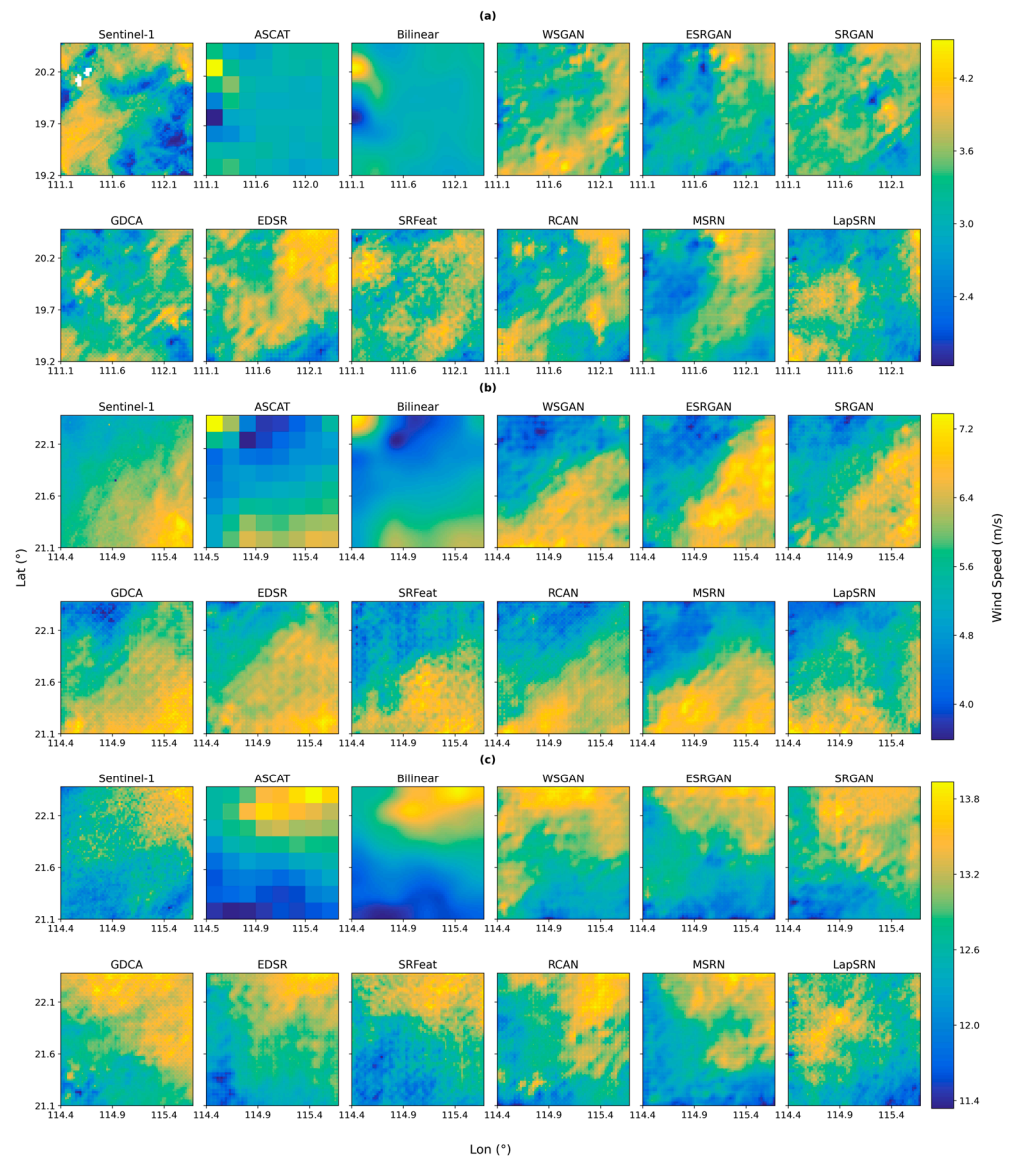
Figure 3. HR OSWS of the collocation region of ASCAT and Sentinel-1 reconstructed by different methods on (**a**) 28 January 2022, (**b**) 10 April 2022, and (**c**) 18 August 2022, at a scale of 8.

Table 2. The RMSE comparison of the different methods in the collocation region of ASCAT and Sentinel-1.

Models	RMSE (m/s)			
	Overall	0~5 m/s OSWS (3 Scenarios)	5~10 m/s OSWS (8 Scenarios)	10~15 m/s OSWS (2 Scenarios)
WSGAN	0.81	0.93	0.84	0.54
ESRGAN	0.86	1.11	0.85	0.57
SRGAN	1.04	1.08	1.12	0.71
GDCA	0.87	1.02	0.87	0.61
SRFeat	0.85	1.09	0.83	0.54
EDSR	0.92	1.15	0.94	0.54
RCAN	0.84	0.99	0.87	0.47
MSRN	0.82	0.95	0.87	0.45
LapSRN	1.03	1.27	1.07	0.59
Bilinear	1.13	1.32	1.16	0.72

Table 3. The MAE comparison of the different methods in the collocation region of ASCAT and Sentinel-1.

Models	MAE (m/s)			
	Overall	0~5 m/s OSWS (3 Scenarios)	5~10 m/s OSWS (8 Scenarios)	10~15 m/s OSWS (2 Scenarios)
WSGAN	0.68	0.80	0.71	0.39
ESRGAN	0.73	0.99	0.71	0.43
SRGAN	0.89	0.95	0.95	0.56
GDCA	0.73	0.90	0.74	0.45
SRFeat	0.72	0.99	0.70	0.38
EDSR	0.79	1.02	0.81	0.40
RCAN	0.71	0.88	0.73	0.34
MSRN	0.69	0.84	0.72	0.32
LapSRN	0.90	1.13	0.92	0.45
Bilinear	0.93	1.19	0.93	0.53

Table 4. The SMAPE comparison of the different methods in the collocation region of ASCAT and Sentinel-1.

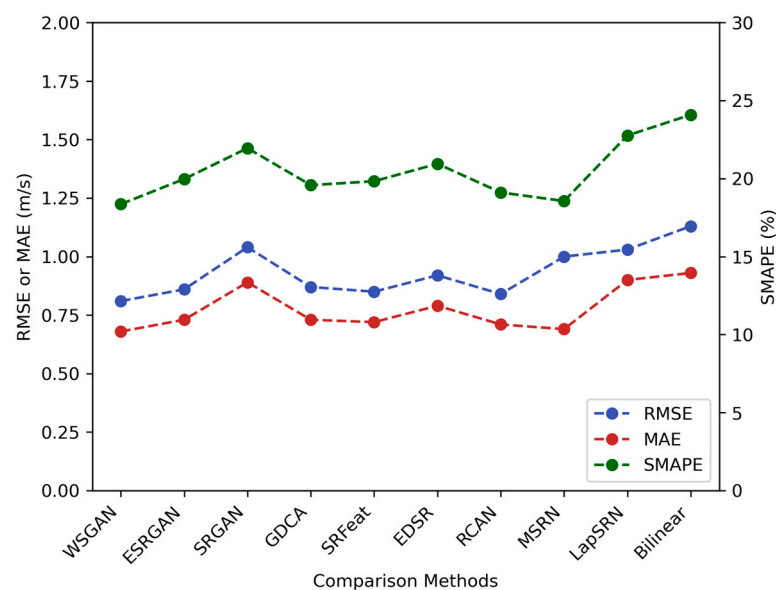| Models	SMAPE (%)			
	Overall	0~5 m/s OSWS (3 Scenarios)	5~10 m/s OSWS (8 Scenarios)	10~15 m/s OSWS (2 Scenarios)
WSGAN	18.36	43.50	12.63	3.58
ESRGAN	19.97	50.18	12.67	3.89
SRGAN	21.95	48.56	16.22	4.96
GDCA	19.58	46.96	13.19	4.08
SRFeat	19.83	50.46	12.44	3.46
EDSR	20.95	51.11	13.95	3.68
RCAN	19.11	46.35	12.88	3.12
MSRN	18.56	44.58	12.70	2.94
LapSRN	22.76	53.75	15.79	4.13
Bilinear	24.09	55.70	17.08	4.71

Figure 4. The accuracy comparison of the different methods in the collocation region of ASCAT and Sentinel-1.

The evaluation of the OSWS super-resolution map is based on the reference resampled high-resolution ERA-5 reanalysis OSWS rather than the resampled OSWS derived from the SAR data observed by the Sentinel-1 satellite. The reason is that the ERA-5 reanalysis OSWS is more reliable than the Sentinel-1 L2 wind speed product. The proposed method aims to comprehend the detailed spatial attributes of high-resolution wind speed retrieval from the Sentinel-1 SAR image while keeping the advantage of the high accuracy of scatterometer OSWS. Furthermore, in the absence of on-site buoy data, most wind speed retrieval studies adopt ERA-5 reanalysis OSWS as the benchmark for accuracy assessment, irrespective of whether the data source is a SAR with high resolution or a scatterometer with relatively low resolution. Therefore, we calculate the RMSE to depict the model's performance. Similarly, in terms of perceptual evaluation of the OSWS super-resolution result, selecting a suitable reference for analyzing image similarity is challenging. Merely resampling ERA-5 reanalysis OSWS fails to introduce additional spatial information and texture features. Consequently, the structural and textural information of ERA-5 reanalysis OSWS does not align with the high-resolution result, rendering comparisons inappropriate. In contrast, the spatial information of Sentinel-1 OSWS corresponds to the scale of high-resolution results. However, SAR's relatively "unreliable" OSWS retrieval result hinders its suitability as a credible reference compared to ERA-5 reanalysis OSWS. Thus, the perceptual accuracy of the image was assessed by visually examining checkerboard artifacts and detailed texture information in this study.

The original resolution of ASCAT OSWS is too coarse to capture fine details. The conventional bilinear interpolation method [41] encounters challenges in reconstructing the comprehensive information of ASCAT OSWS, leading to overly smoothed textures that may not adequately represent subtle variations in the wind field. The 13 test scenarios are divided into categories based on OSWS segments, with three scenarios in the 0~5 m/s, eight in the 5~10 m/s, and two in the 10~15 m/s. The conventional bilinear interpolation method has shown the lowest accuracy in different OSWS segments with the lowest overall RMSE of 1.13 m/s, the lowest overall MAE of 0.93 m/s, and the lowest overall SMAPE of 24.09%. In contrast, GAN-based methods exhibit better performance, showcasing their well-spatial feature extraction and detailed reconstruction capabilities. WSGAN demonstrates optimal performance with an overall RMSE of 0.81 m/s, an overall MAE of 0.68 m/s, and an overall SMAPE of 18.36%. The performance within each OSWS segment is stable, with optimal or suboptimal accuracies. Benefiting from the specialized lightweight architecture and feature loss function, the results in each test area display more comprehensive wind field textures and fewer noticeable checkerboard artifacts. Among the comparison GAN models, the LapSRN and SRGAN exhibit worse accuracies in each OSWS segment, achieving overall RMSE of 1.03 m/s and 1.04 m/s, respectively. Compared with the GAN model with the best performance, the overall RMSE of SRGAN and LapSRN are 0.23 m/s and 0.22 m/s lower, respectively. EDSR, due to its extremely deep network architecture, encounters difficulties in training on OSWS datasets, leading to inferior performance compared to GAN variants, which achieves an overall RMSE of 0.92 m/s, an overall MAE of 0.79 m/s, and an overall SMAPE of 18.36%. The remaining GAN variants show improved overall accuracy compared to the original SRGAN but still fall slightly behind WSGAN. Regarding SRFeat, it achieves an overall RMSE of 0.85 m/s, an overall MAE of 0.72 m/s, and an overall SMAPE of 19.83%. It outperforms the comparison GAN-based model in the 5~10 m/s OSWS segment while inferior to WSGAN, ESRGAN, MSRN, and RCAN within the 0~5 m/s OSWS segment. For MSRN, it achieves an overall RMSE of 0.82 m/s, an overall MAE of 0.69 m/s, and an overall SMAPE of 18.56%. It exhibits good performance within the 10~15 m/s OSWS segment. Regarding the perceptual accuracy evaluation results shown in Figure 2 for three test samples at different OSWS segments, the results of the above comparison GAN-based model exhibit varying degrees of noticeable checkerboard artifacts, which should not be overlooked. Among them, the GDCA model exhibits the most serious checkerboard artifacts. Although SRFeat and MSRN models achieve the top three overall

accuracies in OSWS inversion, there is a visible gap in detail description compared with the proposed WSGAN model.

Overall, the accuracy of each model increases with higher OSWSs in this study. As presented in Tables 2–4, it is evident that within the low OSWS segment (0~5 m/s), the OSWS retrieval accuracy of all the comparison methods is comparatively deficient. WS-GAN exhibits the best performance, with an RMSE of 0.93 m/s and a SMAPE of 43.50%, while the bilinear interpolation method performs the worst, with an RMSE of 1.32 m/s and a SMAPE of 55.70%. Various methods appear to perform poorly according to the evaluation of SMAPE, but this is understandable. The observation of wind speeds below five m/s inherently involves a considerable degree of uncertainty. Taking a real wind speed of 3 m/s as an example, a deviation of 1.5 m/s results in a 50% discrepancy, which may appear substantial. Consequently, there are two distinct metrics for wind speed retrieval: RMSE is utilized for lower wind speeds, while the mean absolute percentage error is considered when the wind speed exceeds 25 m/s. Typically, the overall inversion accuracy of the scatterometer within 10% or 1.5 m/s is considered a reasonable accuracy. Nevertheless, with the increase of OSWS within the moderate OSWS segments (5~10 m/s and 10~15 m/s), the accuracy of each method progressively ameliorates. The fundamental rationale for this phenomenon is that the increase of OSWS leads to heightened roughness of the ocean surface, and the backscatter coefficient of the scatterometer rises in tandem with the increasing roughness of the ocean surface. During low OSWS, the ocean surface exhibits reduced roughness, culminating in a diminished backscatter coefficient for scatterometers. This engenders a diminished acuteness to sea surface roughness and, consequently, a diminished precision in OSWS retrieval. Conversely, in moderate OSWS segments, concomitant with moderate roughness of the ocean surface, an augmentation in wind speed begets a rise in sea surface roughness and a corresponding augmentation in the backscatter coefficient. This culminates in an elevated accuracy in scatterometer wind speed retrieval.

3.2. Evaluation of the Generalization Capability of WSGAN

Further tests were conducted on WindRAD L1 data to assess the generalization capability of WSGAN. Using the maximum likelihood method, the CMOD7 model was employed to invert wind speed from the WindRAD L1 data. Subsequently, the retrieved wind speed images were divided into 8 × 8 patches, a total of 4387, and HR wind speed images were generated using GAN models.

Figure 5 illustrates the distribution map of HR OSWS cumulative errors. Overall, the WSGAN model exhibits good generalization capability in WindRAD. WSGAN outperforms other GAN models, achieving an overall accuracy of 1.11 m/s. However, compared to the testing results obtained from ASCAT, all models demonstrate lower accuracy on WindRAD. There are several main reasons for this disparity. First, the experimental area tested using WindRAD data is larger than the training data. Consequently, the models may struggle to generalize well for regions where historical information has not been learned. Second, wind speed retrieval errors could occur when retrieving OSWS from WindRAD L1 data. Although WindRAD is a dual-frequency dual-polarization scatterometer, only C-band VV polarization data was utilized for wind speed inversion to ensure consistency with ASCAT for comparison purposes. The third potential reason is related to the ground truth data. ERA-5 wind speed data, used as the reference, assimilates ASCAT data but not WindRAD data. This assimilation process may introduce discrepancies when evaluating the performance of the models against WindRAD observations.

3.3. Application Potential in Weak Storm Center Location

Figure 6 showcases Typhoon Nalgae, as captured by WindRAD on 30 October 2022, around 09:09 Coordinated Universal Time (UTC). The black pentagon within the figure represents the current center position of the typhoon (117.7° E, 15.7° N), interpolated using 6-h tropical cyclone best-track data provided by theChina Meteorological Administration (CMA). The interval time is below 0.5 h. The red circle within the figure represents the

typhoon center position (117.385° E, 15.385° N) captured by the scatterometer at a resolution of 10 km. In contrast, the red pentagon within the figure represents the typhoon center position (117.335938° E, 15. 335938° N) captured by the scatterometer at a resampled resolution of 1.25 km. The latter is more accurate and finer.
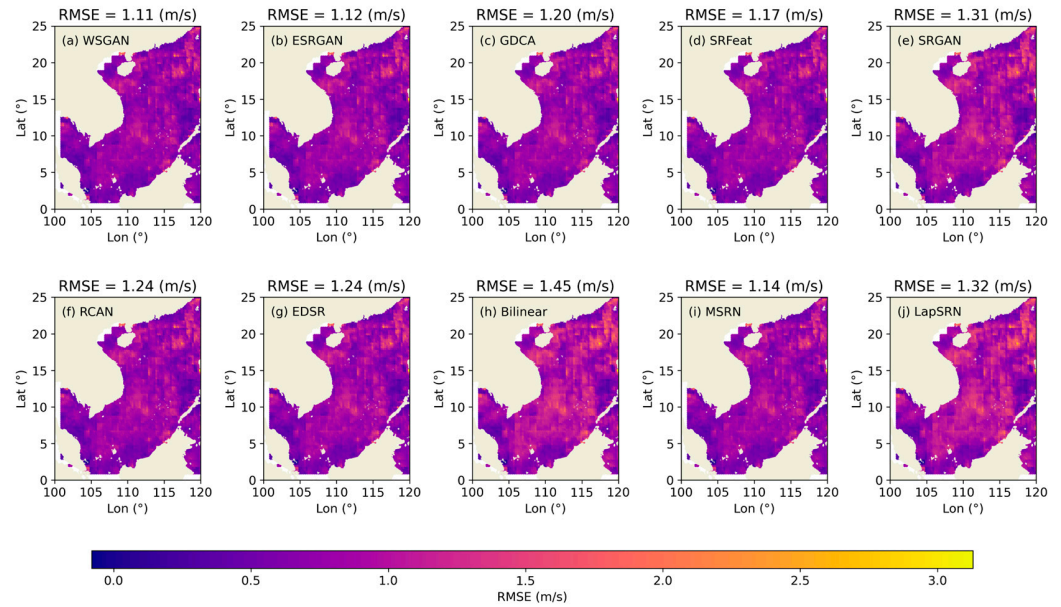

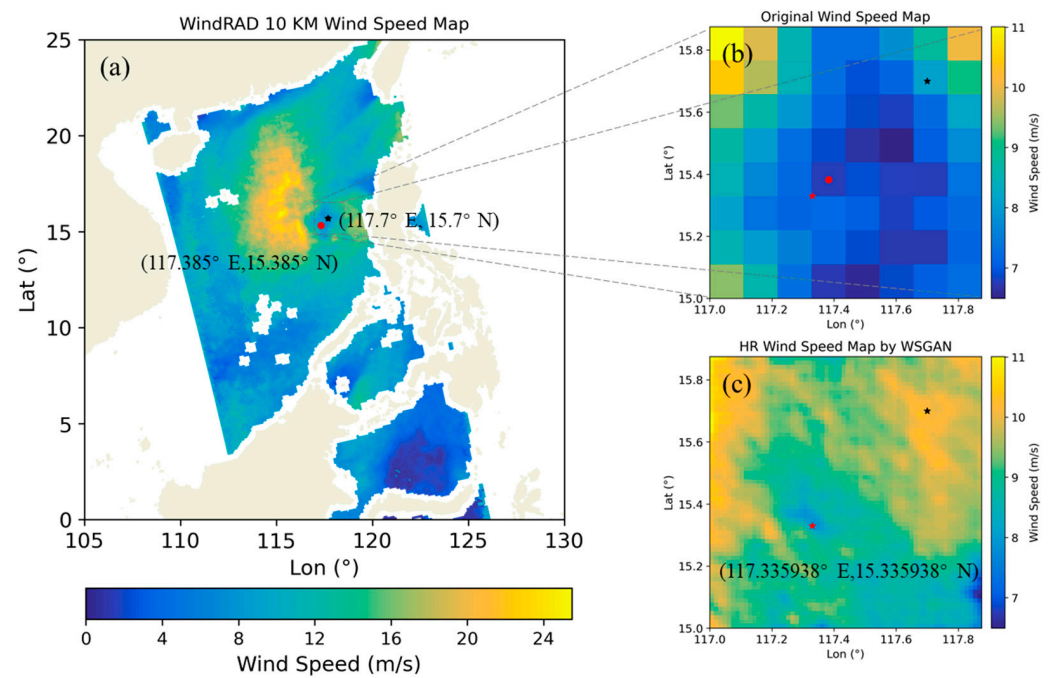**Figure 5.** HR OSWS Error Distribution Map of WindRAD Reconstructed by Different Methods.

Figure 6. Typhoon Nalgae was captured by WindRAD on 30 October 2022, around 09:09 UTC. (**a**) The OSWS retrieval result of WindRAD at 10 km resolution; (**b**) The local OSWS retrieval result around the typhoon center at 10 km resolution; (**c**) The local OSWS retrieval result around the typhoon center at 1.125 km resolution. The black pentagon represents the interpolated center position of the typhoon, using best-track data provided by the CMA, and the red circle and red pentagon represent the typhoon center position captured by the scatterometer at a resolution of 10 km and 1.25 km, respectively.

The scatterometer is capable of capturing the typhoon's eyewall. However, the original coarse resolution struggles to depict finer details. Moreover, the typhoon's movement is variable, making the linearly interpolated typhoon center less accurate. The scatterometer can aid in refining the typhoon's center position, although there remains an error of at least 10 km due to resolution limitations. Fortunately, this error can be partially mitigated by applying super-resolution techniques, such as WSGAN. WSGAN's ability to produce super-resolution wind speed maps ensures that even the most minor variations in wind patterns are captured, enhancing precision and reliability in weather analysis.

3.4. Advantages and Limitations of the Data and Method

The results from the experiment suggest that the proposed approach performs as anticipated. Due to the incorporation of historical spatial information and detailed texture information from high-resolution SAR wind fields during the training process, the GAN models exhibit superior performance compared to the traditional interpolation method. Moreover, the proposed WSGAN model is optimized for OSWS data, including modifications to the generator's and discriminator's architecture, resulting in improved performance. However, there remains a prospect for refining the method. Further enhancements can be applied to the network architecture to rectify specific artifacts. Additionally, the integration of supplementary external data, such as high-resolution brightness temperature data from Soil Moisture Active and Passive (SMAP), which exhibits a discernible correlation with OSWS, holds the potential to introduce more detailed spatial information that could facilitate the reconstruction of high-resolution OSWS.

The commonly used ASCAT data for wind field inversion and the new generation dual-polarization dual-frequency band WindRAD were employed in this research to demonstrate the effectiveness and generalization proficiency of WSGAN. However, the newly launched WindRAD L1 data is available only from 15 March 2022, which leads to insufficient SAR data for spatiotemporal collocation and subsequent training. When sufficient WindRAD data becomes available for training GAN models, designing a multi-channel network that fully leverages the advantages of WindRAD's multi-polarization and multi-frequency band will be possible. This strategic maneuver can potentially elevate the model's performance in reconstructing high-resolution wind fields.

4. Conclusions

This paper designed a GAN-based super-resolution framework incorporating SAR information to generate HR OSWS from LR OSWS retrieved from the scatterometer. Experimental results on ASCAT and WindRAD in the South China Sea demonstrate that GANs, compared to traditional interpolation methods, can enhance the spatial resolution of scatterometer OSWS while introducing additional texture and historical local spatial information. Notably, the WSGAN model outperforms several advanced GAN-based methods across most sea states, exhibiting superior detail extraction with reduced checkerboard artifacts at an eight-fold scale factor. In the collocation region of ASCAT and Sentinel-1, the model achieves an overall RMSE of 0.81 m/s and an overall MAE of 0.68 m/s. It demonstrates excellent generalization capabilities in WindRAD, achieving an overall accuracy of 1.11 m/s. Future research efforts will focus on enhancing the architecture of WSGAN to eliminate artifacts in the reconstructed wind fields.

Institutional Review Board Statement: The paper does not deal with any ethical problems.

References

1. Bentamy, A.; Mouche, A.; Grouazel, A.; Moujane, A.; Mohamed, A.A. Using Sentinel-1A SAR Wind Retrievals for Enhancing Scatterometer and Radiometer Regional Wind Analyses. *Int. J. Remote Sens.* **2019**, *40*, 1120–1147. [CrossRef]
2. Cui, Z.; Pu, Z.; Tallapragada, V.; Atlas, R.; Ruf, C.S. A Preliminary Impact Study of CYGNSS Ocean Surface Wind Speeds on Numerical Simulations of Hurricanes. *Geophys. Res. Lett.* **2019**, *46*, 2984–2992. [CrossRef] [PubMed]
3. Desbiolles, F.; Blanke, B.; Bentamy, A.; Roy, C. Response of the Southern Benguela Upwelling System to Fine-Scale Modifications of the Coastal Wind. *J. Mar. Syst.* **2016**, *156*, 46–55. [CrossRef]
4. Guo, Q.; Xu, X.; Zhang, K.; Li, Z.; Huang, W.; Mansaray, L.R.; Liu, W.; Wang, X.; Gao, J.; Huang, J. Assessing Global Ocean Wind Energy Resources Using Multiple Satellite Data. *Remote Sens.* **2018**, *10*, 100. [CrossRef]
5. Benassai, G.; Di Luccio, D.; Corcione, V.; Nunziata, F.; Migliaccio, M. Marine Spatial Planning Using High-Resolution Synthetic Aperture Radar Measurements. *IEEE J. Ocean. Eng.* **2018**, *43*, 586–594. [CrossRef]
6. De Dominicis, M.; Bruciaferri, D.; Gerin, R.; Pinardi, N.; Poulain, P.M.; Garreau, P.; Zodiatis, G.; Perivoliotis, L.; Fazioli, L.; Sorgente, R.; et al. A Multi-Model Assessment of the Impact of Currents, Waves and Wind in Modelling Surface Drifters and Oil Spill. *Deep. Res. Part II Top. Stud. Oceanogr.* **2016**, *133*, 21–38. [CrossRef]
7. Desbiolles, F.; Bentamy, A.; Blanke, B.; Roy, C.; Mestas-Nuñez, A.M.; Grodsky, S.A.; Herbette, S.; Cambon, G.; Maes, C. Two Decades [1992–2012] of Surface Wind Analyses Based on Satellite Scatterometer Observations. *J. Mar. Syst.* **2017**, *168*, 38–56. [CrossRef]
8. Goodfellow, I.; Pouget-Abadie, J.; Mirza, M.; Xu, B.; Warde-Farley, D.; Ozair, S.; Courville, A.; Bengio, Y. Generative Adversarial Networks. *Commun. ACM* **2020**, *63*, 139–144. [CrossRef]
9. Jozdani, S.; Chen, D.; Pouliot, D.; Alan Johnson, B. A Review and Meta-Analysis of Generative Adversarial Networks and Their Applications in Remote Sensing. *Int. J. Appl. Earth Obs. Geoinf.* **2022**, *108*, 102734. [CrossRef]
10. Ledig, C.; Theis, L.; Huszár, F.; Caballero, J.; Cunningham, A.; Acosta, A.; Aitken, A.; Tejani, A.; Totz, J.; Wang, Z.; et al. Photo-Realistic Single Image Super-Resolution Using a Generative Adversarial Network. In Proceedings of the 30th IEEE Conference on Computer Vision and Pattern Recognition CVPR, Honolulu, HI, USA, 21–26 July 2017; pp. 105–114.
11. Wang, X.; Yu, K.; Wu, S.; Gu, J.; Liu, Y. ESRGAN: Enhanced Super-Resolution Generative Adversarial Networks. In Proceedings of the IEEE Conference on Computer Vision, Munich, Germany, 8–14 September 2018; pp. 63–79.
12. Park, S.J.; Son, H.; Cho, S.; Hong, K.S.; Lee, S. SRFeat: Single Image Super-Resolution with Feature Discrimination. In Proceedings of the 15th European Conference on Computer Vision (ECCV), Munich, Germany, 8–14 September 2018; Volume 11220, pp. 439–455.
13. Nguyen, T.; Hoang, H.; Yoo, C.D. GDCA: GAN-Based Single Image Super Resolution with Dual Discriminators and Channel Attention. *arXiv* **2021**, arXiv:2111.05014.
14. Salaudeen, H.; Çelebi, E. Pothole Detection Using Image Enhancement GAN and Object Detection Network. *Electron* **2022**, *11*, 1882. [CrossRef]
15. Izumi, T.; Amagasaki, M.; Ishida, K.; Kiyama, M. Super-Resolution of Sea Surface Temperature with Convolutional Neural Network-and Generative Adversarial Network-Based Methods. *J. Water Clim. Chang.* **2022**, *13*, 1673–1683. [CrossRef]
16. Pham, V.D.; Bui, Q.T. Spatial Resolution Enhancement Method for Landsat Imagery Using a Generative Adversarial Network. *Remote Sens. Lett.* **2021**, *12*, 654–665. [CrossRef]
17. Zhang, L.; Liu, P.; Wang, L.; Liu, J.; Song, B.; Zhang, Y.; He, G.; Zhang, H. Improved 1-Km-Resolution Hourly Estimates of Aerosol Optical Depth Using Conditional Generative Adversarial Networks. *Remote Sens.* **2021**, *13*, 3834. [CrossRef]
18. Zhu, D.; Cheng, X.; Zhang, F.; Yao, X.; Gao, Y.; Liu, Y. Spatial Interpolation Using Conditional Generative Adversarial Neural Networks. *Int. J. Geogr. Inf. Sci.* **2020**, *34*, 735–758. [CrossRef]
19. Safonova, A.; Ghazaryan, G.; Stiller, S.; Main-Knorn, M.; Nendel, C.; Ryo, M. Ten Deep Learning Techniques to Address Small Data Problems with Remote Sensing. *Int. J. Appl. Earth Obs. Geoinf.* **2023**, *125*, 103569. [CrossRef]
20. Lim, B.; Son, S.; Kim, H.; Nah, S.; Lee, K.M. Enhanced Deep Residual Networks for Single Image Super-Resolution. In Proceedings of the IEEE Computer Society Conference on Computer Vision and Pattern Recognition, Honolulu, HI, USA, 21–26 July 2017; pp. 1132–1140.

21. Zhang, Y.; Li, K.; Li, K.; Wang, L.; Zhong, B.; Fu, Y. Image Super-Resolution Using Very Deep Residual Channel Attention Networks. In Proceedings of the 15th European Conference on Computer Vision (ECCV), Munich, Germany, 8–14 September 2018; Volume 11211, pp. 286–301.

22. Lai, W.S.; Huang, J.B.; Ahuja, N.; Yang, M.H. Deep Laplacian Pyramid Networks for Fast and Accurate Super-Resolution. In Proceedings of the 30th IEEE Conference on Computer Vision and Pattern Recognition CVPR, Honolulu, HI, USA, 21–26 July 2017; pp. 5835–5843.

23. Feng, X.; Li, X.; Li, J. Multi-Scale Fractal Residual Network for Image Super-Resolution. *Appl. Intell.* **2021**, *51*, 1845–1856. [CrossRef]

24. Jiang, B.; Wei, Y.; Ding, J.; Zhang, R.; Liu, Y.; Wang, X.; Fang, Y. Trends of Sea Surface Wind Energy over the South China Sea. *J. Oceanol. Limnol.* **2019**, *37*, 1510–1522. [CrossRef]

25. Stoffelen, A.; Verspeek, J.A.; Vogelzang, J.; Verhoef, A. The CMOD7 Geophysical Model Function for ASCAT and ERS Wind Retrievals. *IEEE J. Sel. Top. Appl. Earth Obs. Remote Sens.* **2017**, *10*, 2123–2134. [CrossRef]

26. Li, Z.; Stoffelen, A.; Verhoef, A.; Wang, Z.; Shang, J.; Yin, H. Higher-order calibration on WindRAD (Wind Radar) scatterometer winds. *Atmos. Meas. Tech.* **2023**, *16*, 4769–4783. [CrossRef]

27. Li, Z.; Verhoef, A.; Stoffelen, A.; Shang, J.; Dou, F. First Results from the WindRAD Scatterometer on Board FY-3E: Data Analysis, Calibration and Wind Retrieval Evaluation. *Remote Sens.* **2023**, *15*, 2087. [CrossRef]

28. De Montera, L.; Remmers, T.; O'Connell, R.; Desmond, C. Validation of Sentinel-1 Offshore Winds and Average Wind Power Estimation around Ireland. *Wind Energy Sci.* **2020**, *5*, 1023–1036. [CrossRef]

29. Hersbach, H.; Bell, B.; Berrisford, P.; Hirahara, S.; Horányi, A.; Muñoz-Sabater, J.; Nicolas, J.; Peubey, C.; Radu, R.; Schepers, D.; et al. The ERA5 Global Reanalysis. *Q. J. R. Meteorol. Soc.* **2020**, *146*, 1999–2049. [CrossRef]

30. Belmonte Rivas, M.; Stoffelen, A. Characterizing ERA-Interim and ERA5 Surface Wind Biases Using ASCAT. *Ocean Sci.* **2019**, *15*, 831–852. [CrossRef]

31. Ni, W.; Stoffelen, A.; Ren, K.; Yang, X. Tropical Cyclone Intensity Estimation From Spaceborne Microwave Scatterometry and Parametric Wind Models. *IEEE J. Sel. Top. Appl. Earth Obs. Remote Sens.* **2022**, *15*, 4719–4729. [CrossRef]

32. Li, X.; Lin, W.; Liu, B.; Wang, Z.; Zhang, B.; He, Y. Sea Surface Wind Retrieval Using the Combined Scatterometer and Altimeter Backscatter Measurements of the HY-2B Satellite. *IEEE Trans. Geosci. Remote Sens.* **2022**, *60*, 5101312. [CrossRef]

33. Wan, Y.; Guo, S.; Li, L.; Qu, X.; Dai, Y. Data Quality Evaluation of Sentinel-1 and Gf-3 Sar for Wind Field Inversion. *Remote Sens.* **2021**, *13*, 3723. [CrossRef]

34. Zhang, B.; Guo, J.; Li, Z.; Cheng, Y.; Zhao, Y.; Yao, F.; Boota, M.W. A Review for Retrieving Wind Fields by Spaceborne Synthetic Aperture Radar. *J. Sens.* **2022**, *2022*, 7773659. [CrossRef]

35. Zhang, B.; Mouche, A.; Lu, Y.; Perrie, W.; Zhang, G.; Wang, H. A Geophysical Model Function for Wind Speed Retrieval from C-Band HH-Polarized Synthetic Aperture Radar. *IEEE Geosci. Remote Sens. Lett.* **2019**, *16*, 1521–1525. [CrossRef]

36. Zheng, M.; Li, X.M.; Sha, J. Comparison of Sea Surface Wind Field Measured by HY-2A Scatterometer and WindSat in Global Oceans. *J. Oceanol. Limnol.* **2019**, *37*, 38–46. [CrossRef]

37. Velo, R.; López, P.; Maseda, F. Wind Speed Estimation Using Multilayer Perceptron. *Energy Convers. Manag.* **2014**, *81*, 1–9. [CrossRef]

38. Escobar, C.A.; Restrepo Alvarez, D. Estimation of Global Ocean Surface Winds Blending Reanalysis, Satellite and Buoy Datasets. *Remote Sens. Appl. Soc. Environ.* **2023**, *32*, 101012. [CrossRef]

39. Flores, J.J.; Cedeño González, J.R.; Rodríguez, H.; Graff, M.; Lopez-Farias, R.; Calderon, F. Soft Computing Methods with Phase Space Reconstruction for Wind Speed Forecasting—A Performance Comparison. *Energies* **2019**, *12*, 3545. [CrossRef]

40. Olaofe, Z.O. A 5-Day Wind Speed & Power Forecasts Using a Layer Recurrent Neural Network (LRNN). *Sustain. Energy Technol. Assess.* **2014**, *6*, 1–24.

41. Watson, S.J.; Kritharas, P.; Hodgson, G.J. Wind speed variability across the UK between 1957 and 2011. *Wind Energy* **2013**, *18*, 21–42. [CrossRef]